# Polar stratospheric nitric acid depletion surveyed from a decadal dataset of IASI total columns

Gaetane Ronsmans[1,a], Catherine Wespes[1,a,*], Lieven Clarisse[1], Susan Solomon[2], Daniel Hurtmans[1], Cathy Clerbaux[1,3], and Pierre-François Coheur[1]

[1]Université libre de Bruxelles (ULB), Spectroscopy, Quantum Chemistry and Atmospheric Remote Sensing (SQUARES), Brussels, Belgium
[2]Department of Earth, Atmospheric and Planetary Sciences, Massachusetts Institute of Technology, Cambridge, Massachusetts, USA
[3]LATMOS/IPSL, Sorbonne Université, UVSQ, CNRS, Paris, France

[*] Corresponding author: Catherine Wespes (catherine.wespes@ulb.be)
[a] Co-first authors

## Abstract

In this paper, we exploit the first 10-year data-record (2008-2017) of nitric acid ($HNO_3$) total columns measured by the IASI-A/Metop infrared sounder, characterized by an exceptional daily sampling and a good vertical sensitivity in the lower-to-mid stratosphere (around 50 hPa), to monitor the relationship between the temperature decrease and the observed $HNO_3$ loss that occurs each year in the Antarctic stratosphere during the polar night. Since the $HNO_3$ depletion results from the formation of polar stratospheric clouds (PSCs) which trigger the development of the ozone ($O_3$) hole, its continuous monitoring is of high importance. We verify here, from the 10-year time evolution of $HNO_3$ together with temperature (taken from reanalysis at 50 hPa), the recurrence of specific regimes in the annual cycle of IASI $HNO_3$ and identify, for each year, the day and the 50 hPa temperature ("drop temperature") corresponding to the onset of strong $HNO_3$ depletion in the Antarctic winter. Although the measured $HNO_3$ total column does not allow the uptake of $HNO_3$ by different types of PSC particles along the vertical profile to be differentiated, an average drop temperature of 194.2 ± 3.8 K, close to the nitric acid trihydrate (NAT) existence threshold (~195 K at 50 hPa), is found in the region of potential vorticity lower than $-10\times10^{-5}$ $K.m^2.kg^{-1}.s^{-1}$ (similar to the 70° – 90° S equivalent latitude region during winter). The spatial distribution and inter-annual variability of the drop temperature are investigated and discussed. This paper highlights the capability of the IASI sounder to monitor the evolution of polar stratospheric $HNO_3$, a key player in the processes involved in the depletion of stratospheric $O_3$.

## 1 Introduction

The cold and isolated air masses found within the polar vortex during winter are associated with a strong denitrification of the stratosphere due to the formation of PSCs (composed of $HNO_3$, sulphuric acid ($H_2SO_4$) and water ice ($H_2O$)) (e.g. Peter, 1997; Voigt et al., 2000; von König, 2002; Schreiner et al., 2003; Peter and Grooß, 2012). These clouds strongly affect the polar chemistry by (1) acting as surfaces for the heterogeneous activation of chlorine and bromine compounds, in turn leading to enhanced O3 destruction (e.g. Solomon, 1999; Wang and Michelangeli, 2006; Harris et al., 2010; Wegner et al., 2012) and by (2) removing gas-phase $HNO_3$ temporarily or permanently through uptake by PSCs and sedimentation of large PSC particles to lower altitudes. The denitrification of the polar stratosphere during winter delays the reformation of $ClONO_2$, a chlorine reservoir, and, hence, intensifies the $O_3$ hole (e.g. Solomon, 1999; Harris et al., 2010; Tritscher et al., 2021). The heterogeneous reaction rates on PSC surfaces and the uptake of $HNO_3$ strongly depend on the temperature and on the PSC particles type. The

PSCs are classified into three different types based on their composition and optical properties: type Ia solid nitric acid trihydrate - NAT ($HNO_3.(H_2O)_3$), type Ib liquid supercooled ternary solution - STS ($HNO_3/H_2SO_4/H_2O$ with variable composition) and type II, crystalline water-ice particles (likely composed of a combination of different chemical phases) (e.g. Toon et al., 1986; Koop et al., 2000; Voigt et al., 2000; Lowe and MacKenzie, 2008). In the stratosphere, they mostly consist of mixtures of liquid/solid STS/NAT particles in varying number densities, with $HNO_3$ being the major constituent of these particles. The large-size NAT particles of low number density are the principal cause of sedimentation (Lambert et al., 2012; Pitts et al., 2013; Molleker et al., 2014; Lambert et al., 2016). The formation temperature of STS ($T_{STS}$) and the thermodynamic equilibrium temperatures of NAT ($T_{NAT}$) and ice ($T_{ice}$) have been determined, respectively, as: ~192 K (Carslaw et al., 1995), ~195.7 K (Hanson and Mauersberger, 1988) and ~188 K (Murphy and Koop, 2005) for typical 50 hPa atmospheric conditions (5 ppmv $H_2O$ and 10 ppbv $HNO_3$). While the NAT nucleation was thought to require pre-existing ice nuclei, hence, temperatures below $T_{ice}$ (e.g. Zondlo et al., 2000; Voigt et al., 2003), recent observational and modelling studies have shown that $HNO_3$ starts to condense in early PSC season in liquid NAT mixtures well above $T_{ice}$ (~4 K below $T_{NAT}$, close to $T_{STS}$) even after a very short temperature threshold exposure (TTE) to these temperatures but also slightly below $T_{NAT}$ after a long TTE, whereas the NAT existence persists up to $T_{NAT}$ (Pitts et al., 2013; Hoyle et al., 2013; Lambert et al., 2016; Pitts et al., 2018). It has been recently proposed that the higher temperature condensation results from heterogeneous nucleation of NAT on meteoritic dust in liquid aerosol (Voigt et al., 2005; Hoyle et al., 2013; Grooß et al., 2014; James et al., 2018; Tritscher et al., 2021). Further cooling below $T_{STS}$ and $T_{ice}$ leads to nucleation of liquid STS, of solid NAT onto ice and of ice particles mainly from STS (type II PSCs) (Lowe and MacKenzie, 2008). The formation of NAT and ice has also been shown to be triggered by stratospheric mountain-waves (Carslaw et al., 1998; Hoffmann et al., 2017). Although the formation mechanisms and composition of STS droplets in stratospheric conditions are well described (Toon et al., 1986; Carslaw et al., 1995; Lowe and MacKenzie, 2008), the NAT and ice nucleation processes still require further investigation (Tritscher et al., 2021). This could be important as the chemistry-climate models (CCMs) generally oversimplify the heterogeneous nucleation schemes for PSC formation (Zhu et al., 2015; Spang et al., 2018; Snels et al., 2019), preventing an accurate estimation of $O_3$ levels.

Over the last few decades, ~~S~~several satellite instruments have measured stratospheric $HNO_3$ ~~over decades~~ (e.g. MLS/UARS (Santee et al., 1999), MLS/Aura (Santee et al., 2007), MIPAS/ENVISAT (Piccolo and Dudhia, 2007), ACE-FTS/SCISAT (Sheese et al., 2017) and SMR/Odin (Urban et al., 2009)). Spaceborne instruments such as the CALIOP/CALIPSO lidar and MIPAS/Envisat measuring in the infrared are capable of detecting and classifying PSC types, allowing their formation mechanisms to be investigated (Lambert et al., 2016; Pitts et al., 2018; Spang et al., 2018, Tritscher et al., 2021 and references therein); these satellite data complement in situ measurements (Voigt et al., 2005) and ground-based lidar (Snels et al., 2019). From these available observational datasets, ~~the~~ $HNO_3$ depletion has been linked to PSC formation and detected below the $T_{NAT}$ threshold (Santee et al., 1999; Urban et al., 2009; Lambert et al., 2016; Ronsmans et al., 2018), but its relationship to PSCs still needs further investigation given the complexity of the nucleation mechanisms that depend on ~~a series of~~ several parameters (e.g. atmospheric temperature, water and $HNO_3$ vapour pressure, time exposure to temperatures, temperature history).

In contrast to the limb satellite instruments mentioned above, the infrared nadir sounder IASI offers a dense spatial sampling of the entire globe, twice a day (Section 2). While it cannot provide a vertical profile of $HNO_3$ similar to that from the limb sounders, IASI provides reliable total column measurements of $HNO_3$ characterized by a maximum sensitivity in the low-middle stratosphere around 50 hPa (20 km) during the dark Antarctic winter (Ronsmans et al., 2016, 2018) where PSCs form (Voigt et al., 2005; Lambert et al., 2012; Spang et al., 2016, 2018). This study aims to explore the 10-year continuous $HNO_3$ measurements from IASI to provide a long-term global picture of depletion and of its dependence ~~to~~ on temperatures during polar winter (Section 3). The temperature corresponding to the onset of the strong depletion in $HNO_3$ records (here referred to as ‘drop temperature’) is identified in Section 4 for each observed year and discussed in the context of previous studies.

## 2 Data

The $HNO_3$ data used in the present study are obtained from measurements of the Infrared Atmospheric Sounding Interferometer (IASI) onboard the Metop-A satellite. IASI measures the Earth’s and atmosphere’s radiation in the thermal infrared spectral range (645 - 2760 $cm^{-1}$), with a 0.5 $cm^{-1}$ apodized resolution and a low radiometric noise (Clerbaux et al., 2009; Hilton et al., 2012). Thanks to its polar sun-synchronous orbit with more than 14 orbits a day and a field of view of four simultaneous footprints of 12 km at nadir, IASI provides global coverage twice a day (9.30 AM and PM mean local solar time). That extensive spatial and temporal sampling in the polar regions is key to this study.

The $HNO_3$ vertical profiles are retrieved on a uniform vertical 1 km grid of 41 layers (from the surface to 40 km with an extra layer above to 60 km) in near-real-time by the Fast Optimal Retrieval on Layers for IASI (FORLI) software, using the optimal estimation method (Rodgers, 2000). Detailed information on the FORLI algorithm and retrieval parameters specific to $HNO_3$ can be found in previous papers (Hurtmans et al., 2012; Ronsmans et al., 2016). For this study, only the total columns (v20151001) are used, considering (1) the low vertical resolution of IASI with only one independent piece of information (full width at half maximum - FWHM - of the averaging kernels of ~30 km), (2) the limited sensitivity of IASI to tropospheric $HNO_3$, (3) the dominant contribution of the stratosphere to the $HNO_3$ total column and (4) the largest sensitivity of IASI in the region of interest, i.e. in the low and mid-stratosphere (from ~70 to ~30 hPa), where the $HNO_3$ abundance is the highest (Ronsmans et al., 2016). The IASI measurements capture the expected ~~variations~~ depletion of $HNO_3$ within the polar night, as illustrated in Fig. 1 that shows examples of vertical $HNO_3$ profiles retrieved within the dark Antarctic vortex (above Arrival Heights) and outside the vortex (above Lauder). The retrieved profiles are shown along with their associated total retrieval error and averaging kernels (the total column averaging kernel and the so-called “sensitivity profile” are also represented; see Ronsmans et al., 2016 for more details). The total column averaging kernel (in black) indicates the sensitivity of the total column measurement to changes in the vertical distribution of $HNO_3$, hence, the altitude to which the retrieved total column is mainly sensitive/representative, while the sensitivity profile indicates the extent to which ~~extent t~~he retrieval at one specific altitude comes from the spectral measurement rather than the apriori. Above Arrival Heights during the dark Antarctic winter, we clearly see depleted $HNO_3$ levels in the low and mid-stratosphere and the altitude of maximum sensitivity at around 30 hPa for this case (values of ~1 along the total column averaging kernel around that level). In contrast, at Lauder, $HNO_3$ levels larger than the a priori are observed in the stratosphere with a larger range of maximum sensitivity. The total columns are associated with a total retrieval error ranging from around 3% at mid- and polar latitudes (except above Antarctica) to 25% above cold Antarctic surface during winter and with a low absolute bias ~~(~~smaller than 12% when compared to ground-based FTIR measurements~~)~~, in polar regions over the altitude range where the IASI sensitivity is the largest~~, when compared to ground-based FTIR measurements~~ (see Hurtmans et al., 2012 and Ronsmans et al., 2016 for more details). The highest error measured over the Antarctic arises from ~~(due to~~ a weaker sensitivity above very cold surface with a degrees of freedom for signal (DOFS) of 0.95 and ~~to~~from a poor knowledge of the seasonally and wavenumber-dependent emissivity above ice surfaces, which induces larger forward model errors)~~, and a low absolute bias (smaller than 12%) in polar regions over the altitude range where the IASI sensitivity is the largest, when compared to ground-based FTIR measurements (see Hurtmans et al., 2012 and Ronsmans et al., 2016 for more details)~~. In order to expand on the comparisons against FTIR measurements, which cannot be made during the polar night, Fig. 2 (top panel) presents the time series of daily IASI total $HNO_3$ columns co-located with MLS measurements within 2.5°x2.5° grid boxes, averaged in the 70°S–90°S equivalent latitude band. In order to account for the vertical sensitivity of IASI, the averaging kernels associated with each co-located IASI retrieved profile~~s~~ were applied to the MLS profiles for this cross-comparison. The MLS mixing ratio ~~VMR~~ profiles over the 215-1.5 hPa pressure range were first interpolated to the FORLI pressure grids and extended down to the surface by using the FORLI-HNO3 a priori profile, and then converted into partial columns. Similar variations in the $HNO_3$ column are captured by the two instruments, with an excellent agreement in particular for the timing of the strong $HNO_3$ depletion within the inner vortex core. Note that a similar good agreement between the two satellite datasets is obtained in other latitude bands (see Fig. 2 bottom panel for the 50°S–70°S equivalent latitude band; the other bands are not shown).

Quality flags similar to those developed for $O_3$ in previous IASI studies (Wespes et al., 2017) were applied a posteriori to exclude data (i) with a corresponding poor spectral fit (e.g. based on quality flags rejecting biased or sloped residuals, fits with maximum number of iteration exceeded), (ii) with less reliability (e.g. based on quality flags rejecting suspect averaging kernels, data with less sensitivity characterized by a DOFS lower than 0.9) or (iii) with tropospheric cloud contamination (defined by a fractional cloud cover ≥ 25 %). Note that the $HNO_3$ total column distributions illustrated in sections below use the median as a statistical average since it is more robust against the outliers than the mean.

Temperature and potential vorticity (PV) fields are taken from the ECMWF ERA Interim Reanalysis dataset, respectively at 50 hPa and at the potential temperature of 530 K (corresponding to ~20 km altitude where the IASI sensitivity to $HNO_3$ is the highest during the Southern Hemisphere (S.H.) winter (Ronsmans et al., 2016)). Because the $HNO_3$ uptake by PSCs starts within a few degrees below $T_{NAT}$ (~195.7 K at 50 hPa (Hanson and Mauersberger, 1988)) depending on the meteorological conditions (Pitts et al., 2013; Hoyle et al., 2013; Lambert et al., 2016; Pitts et al., 2018), a threshold temperature of 195 K is considered in the sections below to identify regions of potential PSC existence. The potential vorticity is used to delimit dynamically consistent areas in the polar regions. In what follows, we use either the equivalent latitudes ("eqlat", calculated from PV fields at 530 K) or the PV values to characterize the relationship between $HNO_3$ and temperatures in the cold polar regions. Uncertainties in ERA-Interim temperatures will also be discussed below.

## 3 Annual cycle of $HNO_3$ vs temperatures

Figure 3a shows the yearly $HNO_3$ cycle (solid lines, left axis) in the southernmost equivalent latitudes (70° - 90° S) as measured by IASI over the whole study period (2008–2017). The total $HNO_3$ variability in such equivalent latitudes has already been discussed in a previous IASI study (Ronsmans et al., 2018), where the contribution of the PSCs to the $HNO_3$ variations was highlighted. The temperature time series, taken at 50 hPa, is represented as well (dashed lines, right axis). From this figure, different regimes of $HNO_3$ total columns *vs* temperature can be observed throughout the year and from one year to another. In particular, we define here three main regimes (R1, R2 and R3) during the $HNO_3$/temperature annual cycle. The full cycle and the main regimes in the 70° - 90° S eqlat region are further represented in Fig. 3b that shows a histogram of the $HNO_3$ total columns as a function of temperature for the year 2011. Similar histograms are observed for the ~~ten~~ other years ~~of IASI measurements~~in the 10-year study period (not shown). The ~~red~~ orange horizontal and vertical lines in Fig. 3a and Fig. 3b, respectively, represent the 195 K threshold temperature used to identify the onset of $HNO_3$ uptake by PSCs (see Section 2). The three ~~identified~~ regimes ~~correspond to~~identified are:

- R1 is defined by the maxima in the total $HNO_3$ abundances covering the months of April and May (~$3\times10^{16}$ molec.cm$^{-2}$), when the 50 hPa temperature strongly decreases (from ~220 to ~195 K). These high $HNO_3$ levels result from low sunlight, preventing photodissociation, along with the heterogeneous hydrolysis of $N_2O_5$ to $HNO_3$ during autumn before the formation of polar stratospheric clouds (Keys et al., 1993; Santee et al., 1999; Urban et al., 2009; de Zafra and Smyshlyaev, 2001). This period also corresponds to the onset of the development of the southern polar vortex, which is characterized by strong diabatic descent with weak latitudinal mixing across its boundary, isolating polar $HNO_3$-rich air from lower-latitude airmasses. The end of the R1 period marks the start of the strong total $HNO_3$ decrease that intensifies later in R2.

- R2, which extends from June to October, follows the onset of the strong decrease in $HNO_3$ total columns ~~which~~ that starts around mid-May in most years when the temperatures fall below 195 K. After a steep initial decline in total $HNO_3$, ~~and~~ R2 is characterized by a plateau of total $HNO_3$ minima. ~~In~~For much of this regime, average $HNO_3$ total columns are below $2\times10^{16}$ molec.cm$^{-2}$ and the 50 hPa temperatures range mostly between 180 and 190 K.

- R3 starts in October when sunlight returns and the 50 hPa temperatures rise above 195 K. Despite 50 hPa temperatures increasing up to 240 K in summer, the $HNO_3$ total columns stagnate at the R2 plateau levels (around $1.5\times10^{16}$ molec.cm$^{-2}$). This regime likely reflects the photolysis of $NO_3$ and $HNO_3$ itself (Ronsmans et al., 2018) as well as the permanent denitrification of the mid-stratosphere, caused by sedimentation of PSCs. The likely renitrification of the lowermost stratosphere (e.g. Braun et al., 2019; Lambert et al., 2012), where the $HNO_3$ concentrations and the IASI sensitivity to $HNO_3$ are lower (Ronsmans et al., 2016), cannot be inferred from the IASI total column measurements. The plateau lasts until approximately February, when $HNO_3$ total column slowly starts increasing, reaching the April-May maximum in R1.

As illustrated in Fig. 3a, the three regimes are observed each year with, however, some interannual variations. For instance, the sudden stratospheric warming (SSW) that occurred in 2010 (see the temperature time series at 20 hPa for the year 2010; green dotted line) yielded higher $HNO_3$ total columns (see green solid line in July - September) (de Laat and van Weele, 2011; Klekociuk et al., 2011; WMO, 2014; Ronsmans et al., 2018).

Figure 3c shows the evolution of the relationship between the daily averaged $HNO_3$ (calculated from a 7-day moving average) with the highest occurrence (in bins of $0.1\times10^{16}$ molec.cm$^{-2}$ and of 2K) and the 50 hPa temperature, over the 10~~-~~year~~s~~ study period ~~of IASI~~. The red vertical line represents the 195 K threshold temperature. ~~Figure 3c clearly illustrates the slow increase in $HNO_3$ columns as the temperatures decrease (February to May, i.e. R3 to R1), the strong and rapid $HNO_3$ depletion occurring in June (R2), and the plateau of low $HNO_3$ abundances in winter and spring (from July to November; R2 to R3).~~ Figure 3c also highlights a large interannual variability in total $HNO_3$ in R3, while the strong depletion in $HNO_3$ in R2 is consistent every year ~~(beginning of June when the temperatures fall below 195 K as indicated by the red vertical line)~~. Given that PSC formation spans a large range of altitudes (typically between 10 and 30 km) (Höpfner et al., 2006, 2009; Spang et al., 2018; Pitts et al., 2018) and that IASI has maximum sensitivity to $HNO_3$ around 50 hPa (Hurtmans et al., 2012; Ronsmans et al., 2016), the temperatures at two other pressure levels, namely 70 and 30 hPa (i.e. ~15 and ~25 km), have also been tested to investigate the relationship between $HNO_3$ and temperature in the low and mid-stratosphere. The results (not shown here) exhibit a similar $HNO_3$-temperature behavior at the different levels with, as expected, lower and higher temperatures in R2, respectively, at 30 hPa and at 70 hPa (temperatures down to ~180 K at 30 hPa and down to ~185 K at 70 hPa, as compared to temperatures down to ~182 K at 50 hPa, are observed), but still below the NAT formation threshold at these pressure levels ($T_{NAT}$ ~193 K at 30 hPa and ~197 K at 70 hPa) (Lambert et al., 2016). Therefore, the altitude range of maximum IASI sensitivity to $HNO_3$ (see Section 2) is characterized by temperatures that are below the NAT formation threshold at these pressure levels, enabling PSC formation and the denitrification process. Furthermore, the consistency between the 195 K threshold temperature taken at 50 hPa and the onset of the strong total $HNO_3$ depletion seen in IASI data (see Fig. 3a) is in agreement with the largest NAT area that starts to develop in June around 20 km (Spang et al., 2018), which justifies the use of the 195 K temperature at that single representative level in this study.

## 4 Onset of $HNO_3$ depletion and drop temperature detection

To identify the spatial and temporal variability of the onset of the depletion phase, the daily time evolution of $HNO_3$ during the first 10 years of IASI measurements and the temperatures at 50 hPa are explored. In particular, the second derivative of $HNO_3$ total column with respect to time is calculated to detect the strongest rate of decrease seen in the $HNO_3$ time series and to identify its associated day and 50 hPa temperature.

### 4.1 $HNO_3$ vs temperature time series

Figure 4 shows the time series of the second derivative of $HNO_3$ total column with respect to time (blue) and of the temperature (red) averaged in the area of potential vorticity ~~at the potential temperature of 530 K~~ smaller than $-10\times10^{-5}$ $K.m^2.kg^{-1}.s^{-1}$ at the potential temperature of 530 K to encompass the region inside the inner polar vortex where the temperatures are the coldest and the largest depletion of total $HNO_3$ occurs (Ronsmans et al., 2018). The use of that PV threshold value explains the gaps in the time series during the summer when the PV does not reach such low levels, while the time series averaged in the 70°- 90° S eqlat band (dashed blue for the second derivative of $HNO_3$ and grey for the temperature) covers the full year. Note that the $HNO_3$ time series has been smoothed with a simple spline data interpolation function to avoid gaps in order to calculate the second derivative of $HNO_3$ total column with respect to time as the daily second-difference in $HNO_3$ total columns. The horizontal red line shows the 195 K threshold.

As already illustrated in Fig. 3a and Fig. 3c, the strongest rate of $HNO_3$ depletion (i.e. the second derivative minimum) is found around the time that temperatures drop below the 195 K threshold (at exactly or a few days after the detection of the 195 K threshold temperature, particularly for the year 2009), within a few days to a few weeks (4 to 23 days) after total $HNO_3$ reaches its maximum, i.e. between the 11~~2~~th of May (2013) and the 8th of June (2009). The 50 hPa drop temperatures, i.e. the temperature associated with the strongest rate of $HNO_3$ depletion detected from IASI, are ~~detected~~ between 189.2 K and 198.6 K, with ~~an~~the exception ~~for~~ of the year 2014, which shows a drop temperature of 202.8 K. On average over the 10 years of studied IASI measurements, a 50 hPa drop temperature of 194.2 K ± 3.8 K (1σ standard deviation) is found. Knowing that $T_{NAT}$ can be higher or lower depending on the atmospheric conditions and that NAT starts to nucleate from ~2–4 K below $T_{NAT}$ (Pitts et al., 2011; Hoyle et al., 2013; Lambert et al., 2016), the results here tend to demonstrate the consistency between the 50 hPa drop temperature and the PSC existence temperature in that altitude region. Note that the range observed in the 50 hPa drop temperature could reflect variations in the preponderance of one type of PSCs over another from one year to the next. The results further justify the use of the single 50 hPa level for characterizing and investigating the onset of $HNO_3$ depletion from IASI. Nevertheless, given the range of maximum IASI sensitivity to $HNO_3$ around 50 hPa, typically between 70 and 30 hPa (Ronsmans et al., 2016), the drop temperatures are also calculated at these two other pressure levels (not shown here) in order to estimate the uncertainty of the calculated drop temperature defined in this study at 50 hPa. The 30 hPa and 70 hPa drop temperatures range respectively over 185.7 K – 194.9 K and over 194.8 K – 203.7 K, with an average of 192.0 ± 2.9 K and 198.0 ± 3.2 K (1σ standard deviation) over the ten years of IASI. The average values at 30 hPa and 70 hPa fall within the 1σ standard deviation associated with the average drop temperature at 50 hPa. It is also worth noting the agreement between the drop temperatures and the NAT formation threshold at these two pressure levels ($T_{NAT}$ ~ 193 K at 30 hPa and ~197 K at 70 hPa) (Lambert et al., 2016). Finally, it should be noted that, because the size, shape or location of the vortex vary slightly over the altitude range to which IASI is sensitive (from ~30 to ~70 hPa during the polar night), the use of a single potential temperature surface for the calculation of drop temperatures could introduce some uncertainties into the results. However, several tests suggest that these variations of the vortex are overall minor and, hence, ~~could~~ have only ~~have~~ limited influence on the identification~~delimitation~~ of the inner polar vortex (delimited by a PV value of $-10\times10^{-5}$ K.m$^2$.kg$^{-1}$.s$^{-1}$ at 530 K) and on the determination~~detection~~ of the average drop temperature inside that region.

Figures 5a and b show the climatological zonal distribution of $HNO_3$ total columns and of the temperature at 50 hPa, respectively, spanning the 55° S - 90° S geographic latitude band over the first ten years ~~whole~~of IASI ~~period~~, with, superimposed, three isocontour levels of potential vorticity (-10, -8 and $-5\times10^{-5}$ K.m$^2$.kg$^{-1}$.s$^{-1}$ in blue, cyan and black, respectively) and the isocontours for the 195 K temperature (pink) and for the averaged 194.2 K drop temperature (purple) at 50 hPa. They further illustrate the relationship between the IASI total $HNO_3$ columns and the 50 hPa temperatures. The ~~average~~ climatological (2008-2017) PV isocontour of $-10\times10^{-5}$ K.m$^2$.kg$^{-1}$.s$^{-1}$ is clearly shown to separate well the region of strong depletion in total $HNO_3$, ~~-~~according to the latitude and the time, until October. The red vertical dashed line indicates the annual average of the dates on which ~~for~~ the 50 hPa ~~average~~ drop temperatures are calculated in the area of PV≤ $-10\times10^{-5}$ K.m$^2$.kg$^{-1}$.s$^{-1}$ (194.2 ± 3.8 K; see Fig. 4) over the first ten years of IASI ~~period~~. It shows that the strongest rate of $HNO_3$ depletion occurs on average at the end of May (24 May), a few days after the temperature decreases below 195 K. ~~The delay between the maximum in total $HNO_3$ and the start of the depletion (see Fig. 4) is also visible in Fig. 5a. For the purpose of the illustrations, t~~The yearly zonally averaged time series over the 10-~~ten-~~years study period~~of IASI~~ can be found in Fig. 6, which shows that IASI measures similar $HNO_3$ total column zonal distributions every year, in particular with respect to the edge of the collar region and of the region of strong depletion (respectively delimited by the PV isocontours of $-5\times10^{-5}$ K.m$^2$.kg$^{-1}$.s$^{-1}$ and of $-10\times10^{-5}$ K.m$^2$.kg$^{-1}$.s$^{-1}$ at 530 K. An exact timing or a delay of a few days between the detection of the averaged 195 K threshold temperature and the start of the $HNO_3$ depletion is visible every year in Fig. 6. In particular, the year 2009 shows the longest delay (see also Fig. 4).~~, measured by IASI from year to year, as well as the reproducibility of the NAT threshold temperature region that encompasses the inner vortex core. Except for the year 2009, the dates for the strongest rate of $HNO_3$ depletion matches those for the onset of decreasing temperatures below 195 K.~~ Note that the mismatch observed in the 10-year average between the detection of the averaged 195 K threshold temperature and the average date for the drop temperatures (see Fig. 5 a and b) is driven by the year 2013 which is characterized by the lowest temperatures during the Antarctic winter over the 10-year study period and, hence, the earliest date for the drop temperature (11th of May; see Fig. 4 and Fig. 6).

## 4.2 Spatial ~~D~~distribution of drop temperatures

To explore the capability of IASI to monitor the onset of $HNO_3$ depletion at a large scale, figure 7 shows, for each year of the study period, the spatial distribution of the 50 hPa drop temperatures based on the second derivative minima of total $HNO_3$ averaged in 1°×1° grid cells. The region of interest here is delimited by a PV value of −8×10−5 K.m2.kg−1.s−1 at 530 K, in order to investigate an area a bit larger than the inner vortex core that was the focus of the preceding discussion (delineated in green in figure 7 by the PV isocontour of −10×10–5 K.m2.kg–1.s–1 averaged over the interval 10 May to 15 July). To explore the capability of IASI to monitor the onset of $HNO_3$ depletion at a large scale from year to year, figure 7 shows the spatial distribution of the 50 hPa drop temperatures (based on the second derivative minima of total $HNO_3$ averaged in 1°×1° grid cells) inside a region delimited by a PV value of -8×10$^{-5}$ K.m$^2$.kg$^{-1}$.s$^{-1}$ for each year of the IASI period in order to investigate a region a bit larger than that of the strong depletion in total $HNO_3$ encircled by the PV isocontour of -10×10$^{-5}$ K.m$^2$.kg$^{-1}$.s$^{-1}$, averaged over the 10 May – 15 July period for each year, which delimits our region of interest (in green). The isocontour of -10×10$^{-5}$ K.m$^2$.kg$^{-1}$.s$^{-1}$ for the minimum PV (in cyan) encountered at 530 K over the 10 May to 15 July period for each year, as well as the isocontours of 195 K for the average temperatures and the minimum temperatures, are also represented. The calculated drop temperatures corresponding to the onset of $HNO_3$ depletion inside the averaged PV isocontour are found to vary between ~180 and ~210 K and the corresponding dates range between ~mid-May and mid-July (not shown here). Although the range of drop temperatures and dates for 1°×1° bins is broader than that found for the inner vortex averages discussed above, the results are qualitatively consistent. For example, Tthe year 2014 that shows the highest inner vortex average drop temperature in Figure 4 is characterized by the highest drop temperatures above the eastern Antarctic. Note, however, that the high extremes in the drop temperature, mainly found above the eastern Antarctic, should be considered with caution: they correspond to specific regions above ice surfaces with emissivity features that are known to yield errors in the IASI retrievals (Hurtmans et al., 2012; Ronsmans et al., 2016). Indeed, bright land surfaces such as ice might in some cases lead to poor $HNO_3$ retrievals. Although wavenumber-dependent surface emissivity atlases are used in FORLI (Hurtmans et al., 2012), this parameter remains critical and causes poorer retrievals that, in some instances, pass through the series of quality filters and could affect the drop temperature calculation.

The averaged isocontour of 195 K encircles fairly well the area of $HNO_3$ drop temperatures lower than 195 K (typically from ~187 K to ~195 K), which means that the bins inside that area include airmasses that experience the NAT threshold temperature during a long time over the 10 May – 15 July period. That area encompasses the inner vortex core (delimited by the isocontour of -10×10$^{-5}$ K.m$^2$.kg$^{-1}$.s$^{-1}$ for the PV averaged over the 10 May – 15 July period) and shows pronounced minima (lower than -0.5×10$^{14}$ molec.cm$^{-2}$.d$^{-2}$) in the second derivative of the $HNO_3$ total column with respect to time (not shown here), which indicate a strong and rapid $HNO_3$ depletion. The area enclosed between the two isocontours of 195 K for the temperatures, the averaged one and the one for the minimum temperatures, shows generally higher drop temperatures and weakest minima (larger than -0.5×10$^{14}$ molec.cm$^{-2}$.d$^{-2}$) in the second derivative of the $HNO_3$ total column (not shown). That area is also typically enclosed by the isocontour of -10×10$^{-5}$ K.m$^2$.kg$^{-1}$.s$^{-1}$ for the minimum PV, meaning that the bins inside correspond, at least for one day over the 10 May – 15 July period, to airmasses located at the inner edge of the vortex and characterized by temperature lower than the NAT threshold temperature. The fact that the weakest minima in the second derivative of total $HNO_3$ (not shown) are observed in that area (not shown) indicates a weak and slow $HNO_3$ depletion and that might be explained by air masses at the inner edge of the vortex experiencing only a short period with temperatures below a short period of the NAT threshold temperature experienced at the inner edge of the vortex. It could also reflect mixing with strongly $HNO_3$-depleted and colder airmasses from the inner vortex core. Mixing with these already depleted airmasses could also explain the higher drop temperatures detected in those bins. These sometimes unrealistic high drop temperatures are generally detected later (after the strong $HNO_3$ depletion occurs in the inner vortex core, i.e. after the 10 May – 15 July period considered here – not shown), which supports the transport, in those bins, of earlier previously $HNO_3$-depleted airmasses and the likely mixing at the edge of the vortex. Note, however, that previous studies have shown a generally weak mixing in the Antarctic between the edge region and the vortex core (e.g. Roscoe et al., JGR 2012).

Finally, these spatial variations might also partly reflect some uncertainty in~~to~~ the drop temperature calculation, introduced by the use of temperature at a single pressure level (50 hPa) and of PV on a single potential temperature surface (530 K) while the sensitivity of IASI to changes in the $HNO_3$ profiles extends over a range from ~30 to ~70 hPa during the polar night. It should be noted that biases in the ECMWF ERA Interim temperatures used in this work~~,~~ are too small to explain the large range of drop temperatures calculated here. Indeed, Lambert and Santee (2018) found only a small warm bias, with median differences around 0.5 K, reaching 0–0.25 K in the southernmost regions of the globe at ~68–21 hPa where PSCs form, through comparisons with the Constellation Observing System for Meteorology, Ionosphere and Climate (COSMIC) data.

Except above some parts of Antarctica which are prone to larger retrieval errors and where unrealistic high drop temperatures are found, the overall range in the 50 hPa drop temperature for total $HNO_3$ inside the isocontour for the averaged temperature of 195 K typically extends from ~187 K to ~195 K, which falls within the range of PSC nucleation temperature at 50 hPa: from slightly below $T_{NAT}$ to around 3-4 K below the ice frost point - $T_{ice}$ - depending on atmospheric conditions, on TTE and on the specific formation mechanism (i.e., the type of PSC developing) (Pitts et al., 2011; Peter and Grooß, 2012; Hoyle et al., 2013). This underlines well the benefit of the excellent spatial and temporal coverage of IASI, which allows the rapid and critical depletion phase to be captured in detail over a large scale.

## 5 Conclusions

In this paper, we have explored the added value of the dense $HNO_3$ total column dataset provided by the IASI/Metop-A satellite over a full decade (2008–2017) for monitoring the stratospheric depletion phase that occurs each year in the S.H. and for investigating its relationship to the NAT formation temperature. To that end, we focused on and delimited the coldest polar region of the S.H. using a specific PV value at 530 K (~50 hPa, PV of $-10\times10^{-5}$ $K.m^2.kg^{-1}.s^{-1}$) and stratospheric temperatures at 50 hPa, taken from the ECMWF ERA Interim reanalysis. That single representative pressure level has been considered in this study given the maximum sensitivity of IASI to $HNO_3$ around that level, which lies in the range where the PSCs formation/denitrification processes occur.

The annual cycle of total $HNO_3$, as observed from IASI, has first been characterized according to the temperature evolution. Three regimes (R1 to R3) in the total $HNO_3$ - 50 hPa temperature relationship were highlighted from the time series over the S.H. polar region: R1 is defined during April and May and characterized by a rapid decrease in 50 hPa temperatures while $HNO_3$ accumulates ~~in~~over the pole~~s~~; R2, from June to ~~September~~October, follows the onset of the depletion that starts around mid-May in most years when the 50 hPa temperatures fall below 195 K (considered here as the onset of PSC nucleation phase at that level), with a strong consistency from year to year; R3, defined from October through March when total $HNO_3$ remains at low R2 plateau levels, despite the return of sunlight and heat, characterizes the strong denitrification of the stratosphere, likely due to PSC sedimentation to lower levels where the IASI sensitivity is low. For each year over the 10-year study ~~IASI~~ period, the use of the second derivative of the $HNO_3$ column versus time was then found to be particularly valuable to detect the onset of the $HNO_3$ condensation into PSCs. It is captured, on average from IASI, a few days before June with a delay of 4–23 days after the maximum in total $HNO_3$. The corresponding temperatures ('drop temperatures') were detected between 189.2 K and 202.8 K (194.2 ± 3.8 K on average over the 10 years), which tends to demonstrate the good consistency between the 50 hPa drop temperature and the PSC formation temperatures in that altitude region. Finally, the annual and spatial variability (within 1°× 1°) in the drop temperature was further explored from IASI total $HNO_3$. Inside the isocontours of 195 K for the average temperatures and of $-10\times10^{-5}$ $K.m^2.kg^{-1}.s^{-1}$ for the averaged PV at 530 K, the drop temperatures are detected between ~mid-May and mid-July, typically range between ~187 K to ~195 K and are associated with the lowest minima (lower than $-0.5\times10^{14}$ molec.cm$^{-2}$.d$^{-2}$) in the second derivative of the $HNO_3$ total column with respect to time, indicating a strong and rapid $HNO_3$ depletion. Except for unrealistic~~extreme~~ drop temperatures (~210 K) that were found in some years above eastern Antarctica and suspected to result from unfiltered poor quality retrievals arising from~~in case of~~ emissivity issues above ice, the range of drop temperatures is interestingly found to be in line with the PSC nucleation temperature that is known, from previous studies, to strongly depend on ~~a series of~~several factors (e.g. meteorological conditions, $HNO_3$ vapour pressure, temperature threshold exposure, presence of meteoritic dust). At the edge of the vortex, considering the isocontours of 195 K for the minimum temperatures or of $-10\times10^{-5}$ K.m$^2$.kg$^{-1}$.s$^{-1}$ for the minimum PV, higher and later drop temperatures along with weakest minima in the second derivative of the $HNO_3$ total column with respect to time, indicating a slow $HNO_3$ depletion, are found. These likely result~~s~~ from a short temperature threshold exposure or mixing with already depleted airmasses from the inner vortex core. The results of this study highlight the ability of IASI to measure the variations in total $HNO_3$ and, in particular, to capture and monitor the rapid depletion phase over the whole Antarctic region~~s~~.

We show in this study that the IASI dataset allows the variability of stratospheric $HNO_3$ throughout the year (including the polar night) in the Antarctic to be captured. In that respect, it offers observational means to monitor the relation of $HNO_3$ to temperature and the related formation of PSCs. Despite the limited vertical resolution of IASI which does not allow investigation of the $HNO_3$ uptake by the different types of PSCs during their formation and growth along the vertical profile, the $HNO_3$ total column measurements from IASI constitute an important new dataset for exploring the strong polar depletion over the whole stratosphere. This is particularly relevant considering the mission continuity, which will span several decades with the planned follow-on missions. Indeed, thanks to the three successive instruments (IASI-A launched in 2006 and still operating, IASI-B in 2012, and IASI-C in 2018) that demonstrate an excellent stability of the Level-1 radiances, the measurements will soon provide an unprecedented long-term dataset of $HNO_3$ total columns. Further work could also make use of this unique data set to investigate the relation between $HNO_3$, $O_3$, and meteorology in the changing climate.

## Data availability

The IASI $HNO_3$ data processed with FORLI-$HNO_3$ v0151001 are available upon request to the corresponding author.

## Author contributions

C.W. and G.R. performed the analysis, wrote the manuscript and prepared the figures. ~~C.W. and~~ L.C. contributed to the analysis. ~~C.W.,~~ S.S., P.-F. C. and L.C. contributed to the interpretation of the results. D.H. was responsible for the retrieval algorithm development and the processing of the IASI $HNO_3$ dataset. All authors contributed to the writing of the text and reviewed the manuscript.

## Competing interests

The authors declare no competing interests.

## Acknowledgements

IASI has been developed and built under the responsibility of the Centre National d'Etudes Spatiales (CNES, France). It is flown on board the Metop satellites as part of the EUMETSAT Polar System. The IASI L1 data are received through the EUMETCast near-real-time data distribution service. The research was funded by the F.R.S.-FNRS, the Belgian State Federal Office for Scientific, Technical and Cultural Affairs (Prodex arrangement 4000111403 IASI.FLOW) and EUMETSAT through the Satellite

Application Facility on Atmospheric Composition Monitoring (ACSAF). G. Ronsmans is grateful to the Fonds pour la Formation à la Recherche dans l'Industrie et dans l'Agriculture of Belgium for a PhD grant (Boursier FRIA). L. Clarisse is a research associate supported by the F.R.S.-FNRS. C. Clerbaux is grateful to CNES for financial support. S. Solomon is supported by the National Science Foundation (NSF-1539972). We also would like to thank the three reviewers for their helpful comments and corrections and, in particular, M. Santee for her in-depth reviews, which have substantially improved the paper quality.

## Figure captions

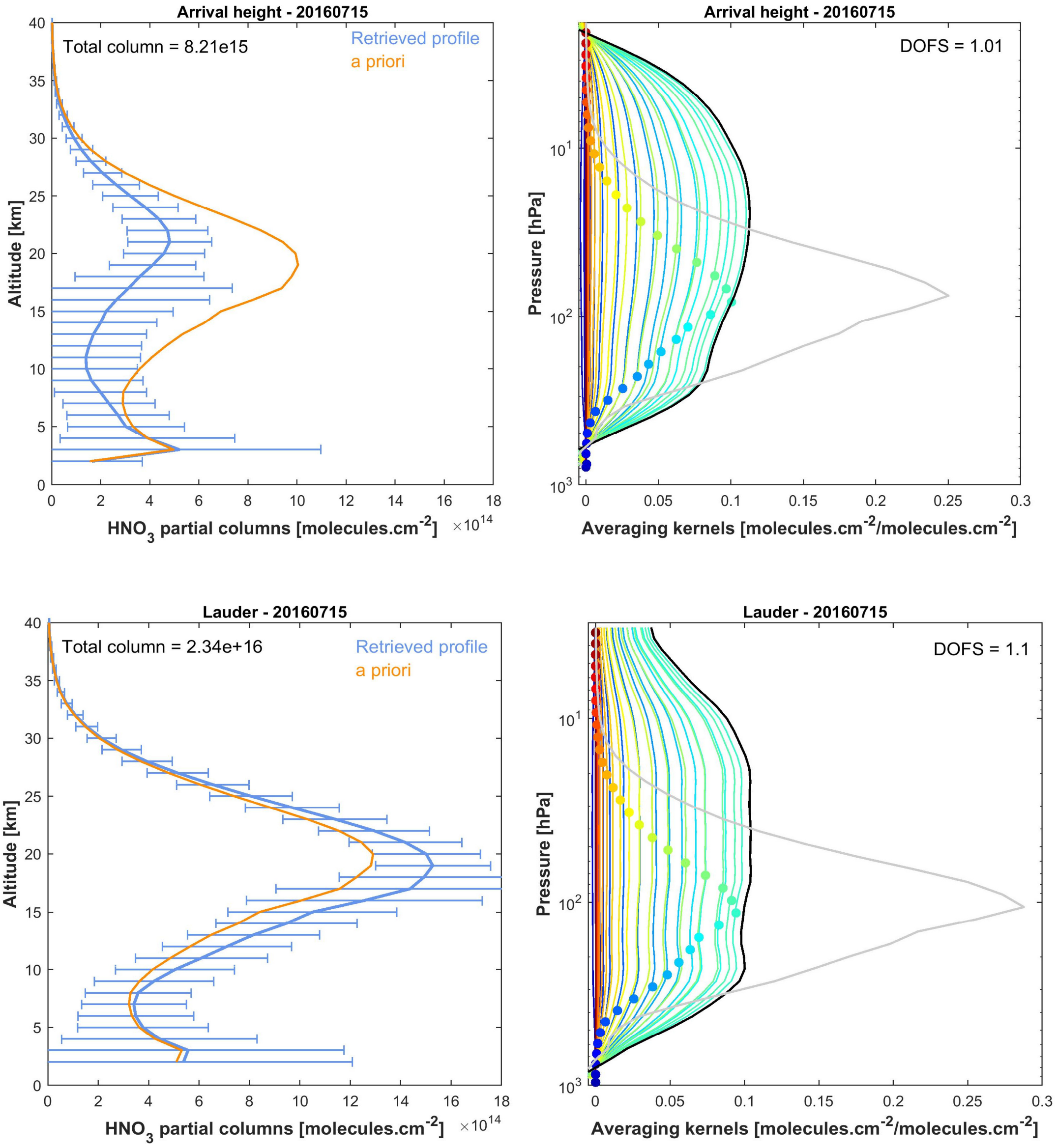


Figure 1. Examples of IASI $HNO_3$ vertical profiles (in molec.cm$^{-2}$) with corresponding averaging kernels (in molec.cm$^{-2}$/molec.cm$^{-2}$; colored lines, with the altitude of each kernel represented by the colored dots) along with the total column averaging kernels (black) and the sensitivity profiles (grey) (both divided by 10) above Arrival Heights (77.49°S, 166.39°E, top panels) and Lauder (45.03°S, 169.40°E; bottom panels). The error bars associated with the $HNO_3$ vertical profile represent the total retrieval error. The a priori profile is also represented. The total column and the DOFS values are indicated.

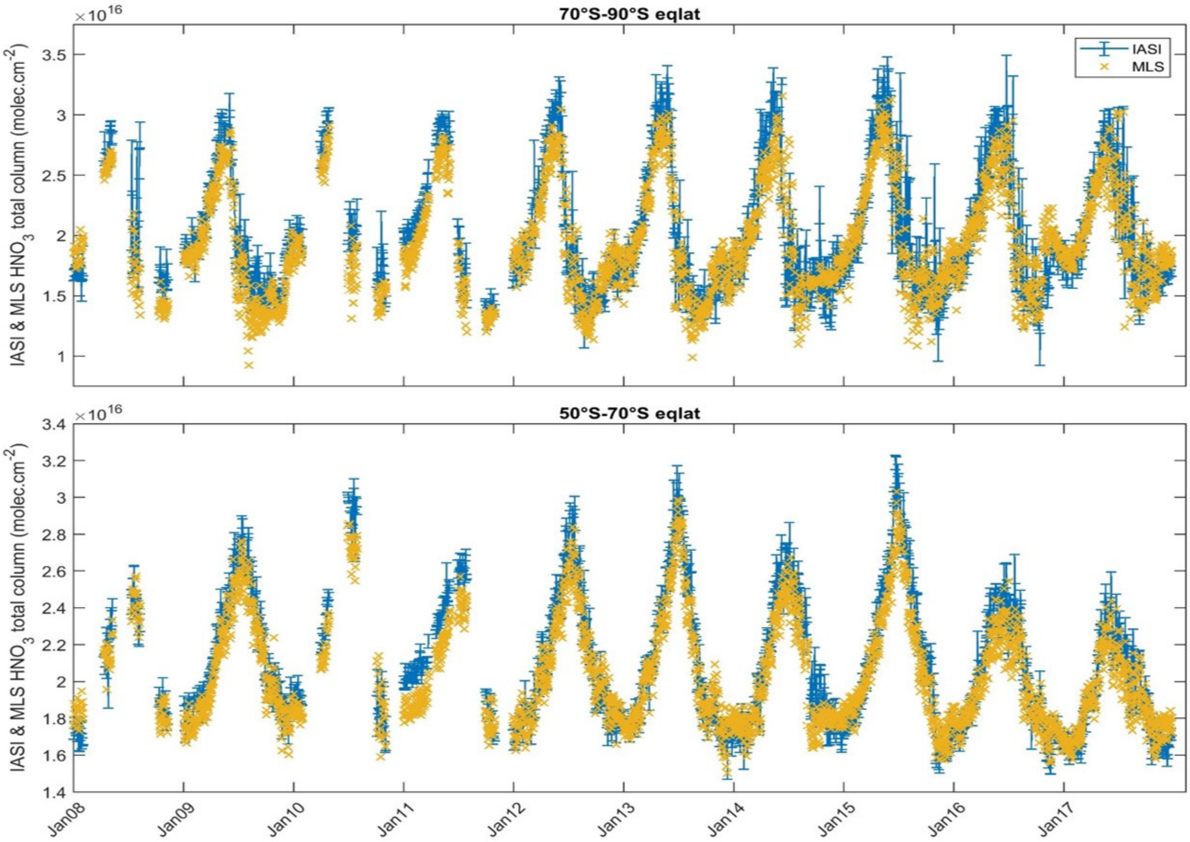


**Figure 2.** Time series of daily IASI total $HNO_3$ column (blue) co-located with MLS and of MLS total $HNO_3$ columns (orange) within 2.5°x2.5° grid boxes, averaged in the 70°S–90°S (top panel) and the 50°S–70°S (bottom panel) equivalent latitude bands. Note that the MLS total column estimates were obtained by extending the MLS partial stratospheric column values using the FORLI-$HNO_3$ a priori information (see text for details). The error bars (blue) represents 3σ, where σ is the standard deviation around the IASI $HNO_3$ daily average.

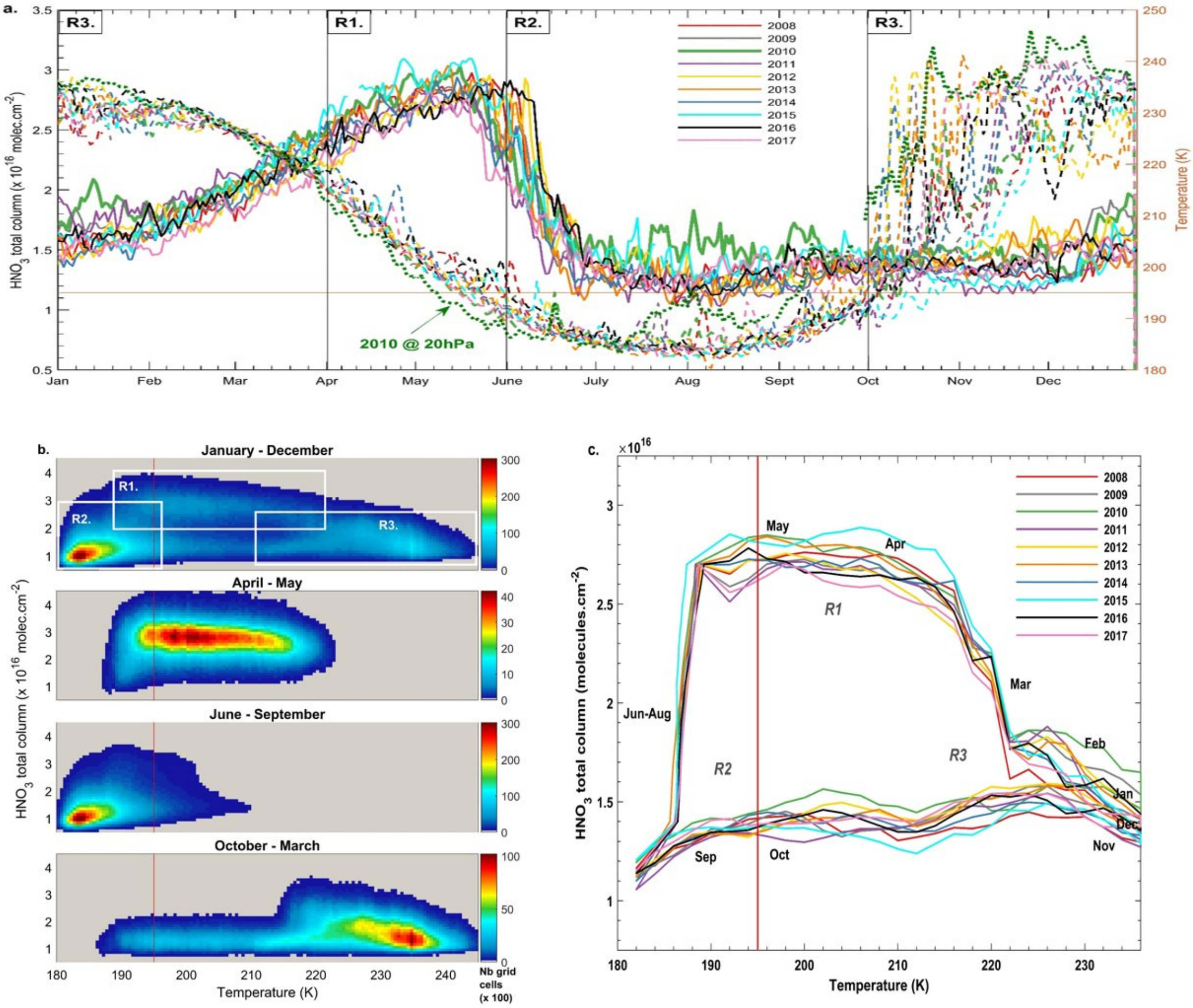
a.
R3.
R1.
R2.
R3.
2008
2009
2010
2011
2012
2013
2014
2015
2016
2017
HNO3 total column (x 10^16 molec.cm^-2)
Temperature (K)
2010 @ 20hPa
Jan
Feb
Mar
Apr
May
June
July
Aug
Sept
Oct
Nov
Dec
b.
January - December
R1.
R2.
R3.
April - May
June - September
October - March
HNO3 total column (x 10^16 molec.cm^-2)
Temperature (K)
Nb grid cells (x 100)
c.
x10^16
May
Apr
R1
Jun-Aug
R2
R3
Mar
Feb
Jan
Dec
Nov
Sep
Oct
HNO3 total column (molecules.cm^-2)
Temperature (K)

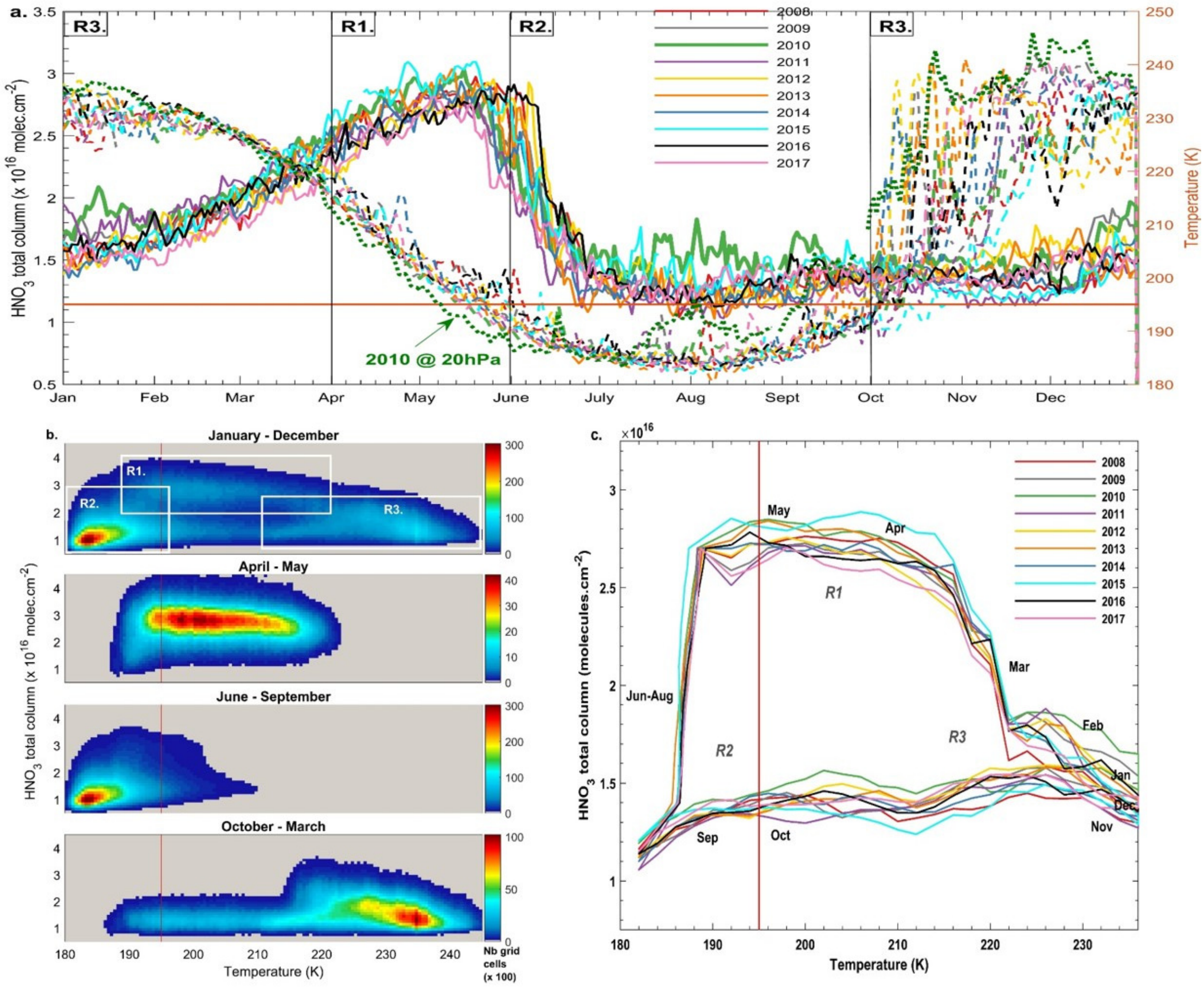


**Figure 3.** (a) Time series of daily averaged $HNO_3$ total columns (solid lines) and temperatures taken at 50 hPa (dashed lines) in the 70° - 90° S equivalent latitude band, for the years 2008 – 2017. The green dotted line represents the temperatures at 20 hPa for the year 2010. (b) $HNO_3$ total columns versus temperatures (at 50 hPa) histogram during the year 2011, ~~for~~ over the whole year (top) and for the 3 defined regimes (R1 - R3) separated in (a) ~~for the year 2011~~. The colors refer to the number of gridded measurements in each cell. (c) Evolution of daily averaged $HNO_3$ total columns with the highest occurrence (in bins of $0.1\times10^{16}$ molec.cm$^{-2}$ and 2 K) as a function of the 50 hPa temperature for the years 2008 – 2017. The ~~red~~ orange horizontal or vertical lines represent the 195 K threshold temperature.

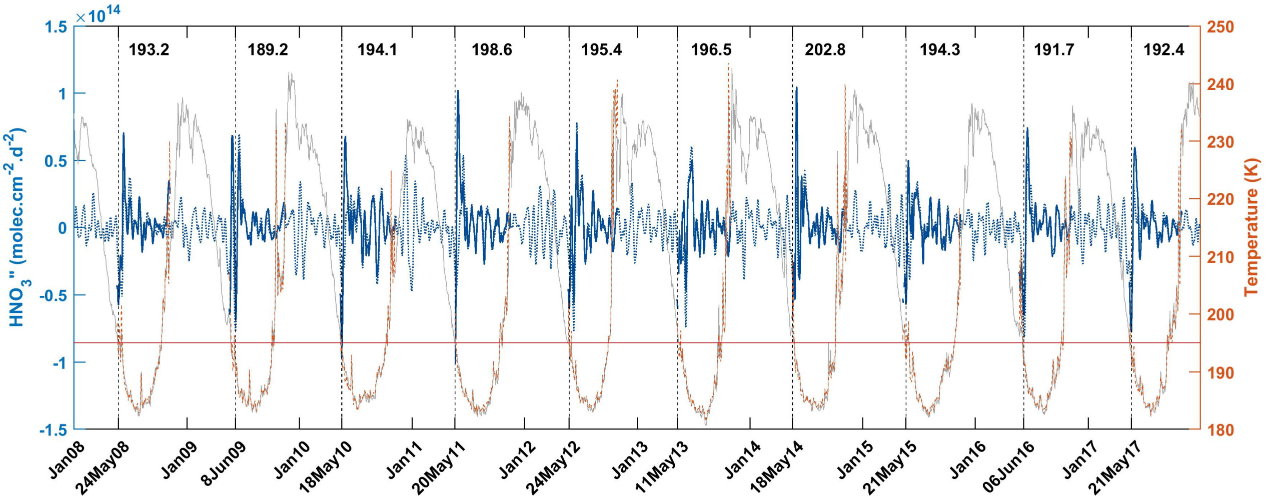


**Figure 4.** Time series of total $HNO_3$ second derivative (blue, left y-axis) and of the 50 hPa temperature (red, right y-axis), in the region of potential vorticity at 530 K lower than $-10\times10^{-5}$ $K.m^2.kg^{-1}.s^{-1}$. The red horizontal line corresponds to the 195 K temperature. The vertical dashed lines indicate the second derivative minimum in $HNO_3$ for each year. The corresponding dates (in bold, on the x-axis) and temperatures are also indicated. The time series of total $HNO_3$ second derivative (dashed blue) and of temperature (grey) in the 70° – 90° S eqlat band are also represented.

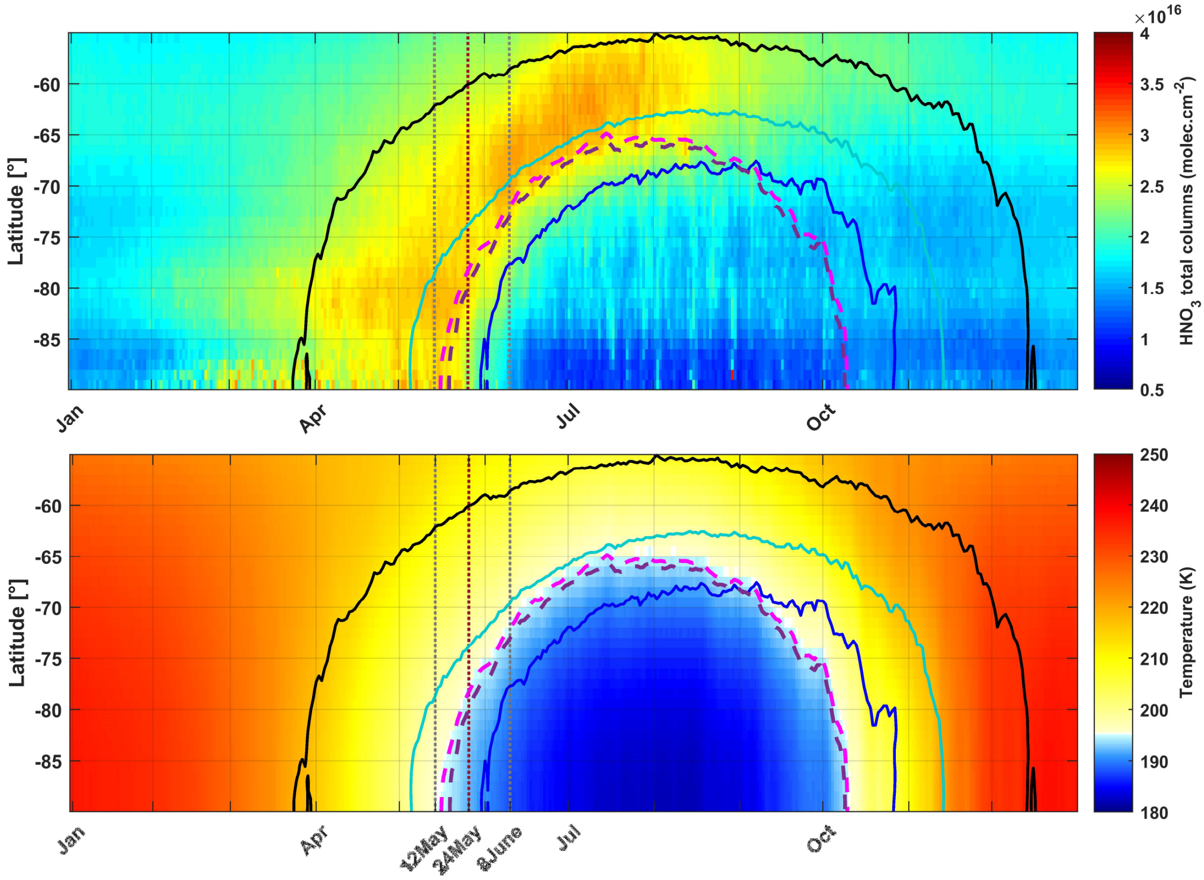
×10^16
HNO3 total columns (molec.cm-2)
Latitude [°]
Temperature (K)
Jan
Apr
Jul
Oct
12May
24May
8June

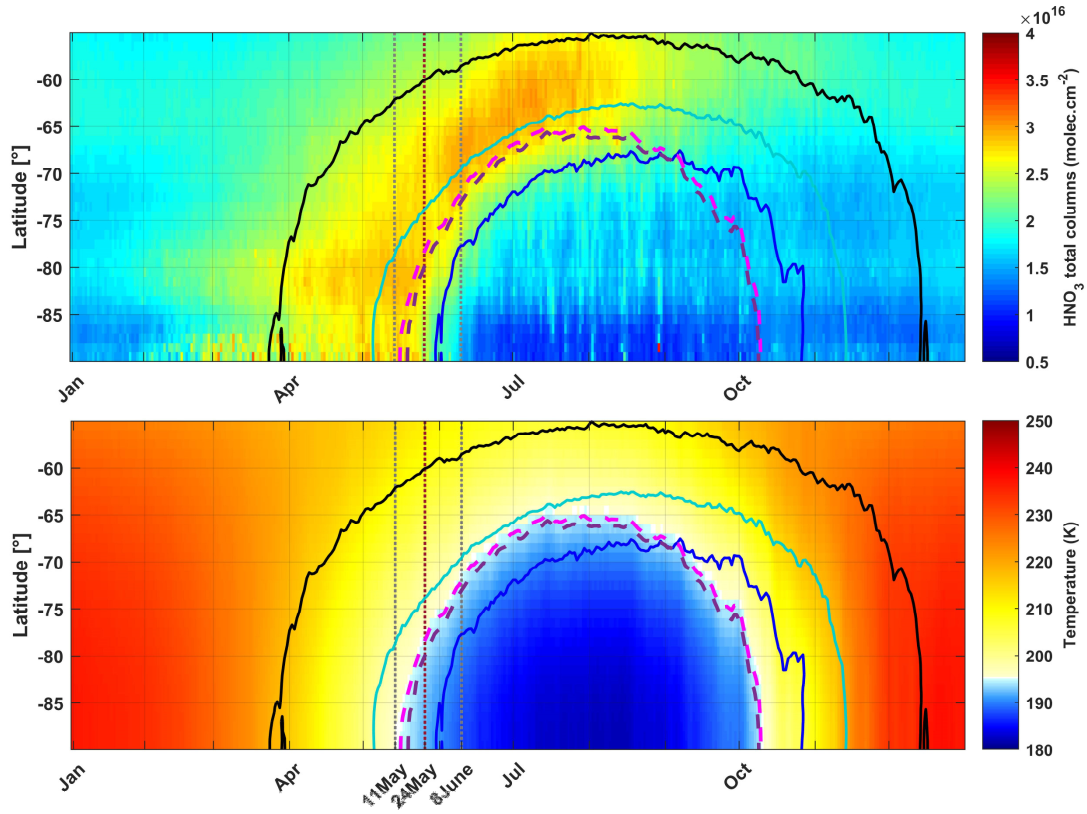


**Figure 5.** Zonal distributions of (a) $HNO_3$ total columns (in molec.cm$^{-2}$) from IASI and (b) temperatures at 50 hPa from ERA Interim (in K) in the 55° S to 90° S geographical latitude band and averaged over the years 2008 – 2017. Three isocontours for the climatological (2008-2017) and zonally averaged PV of -5 (black), -8 (cyan) and -10 (blue) ($\times10^{-5}$ K.m$^2$.kg$^{-1}$.s$^{-1}$) at 530 K, as well as the isocontours for the 195 K climatological (2008-2017) zonally averaged temperature (pink) and for the averaged 194.2 K drop temperature (purple) at 50 hPa are superimposed. The vertical grey dashed lines mark the earliest and latest dates for the averaged drop temperature in the 10-year IASI record and the red one indicates the average date for the drop temperatures calculated in the area delimited by the~~a~~ -10$\times10^{-5}$ K.m$^2$.kg$^{-1}$.s$^{-1}$ PV contour.

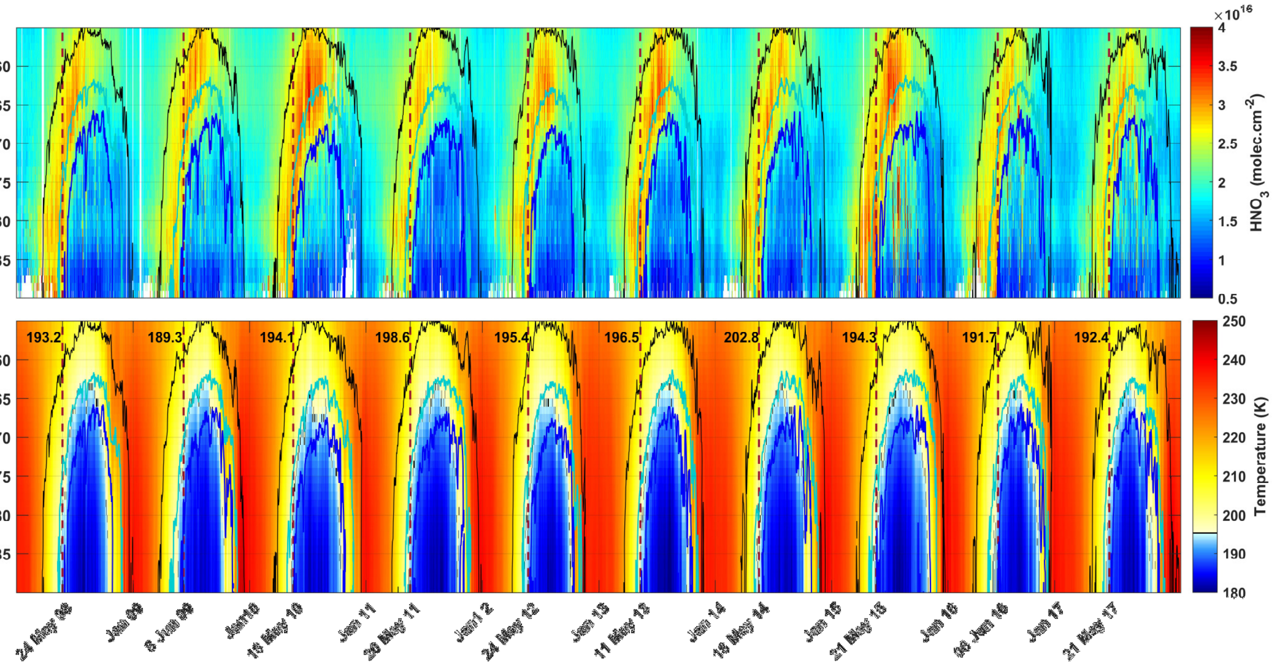


**Figure 6.** Zonally averaged distributions of (top) $HNO_3$ total columns (in molec.cm$^{-2}$) from IASI and (bottom) temperatures at 50 hPa from ERA Interim (in K). The geographical latitude range is from 55° to 90° south and the isocontours are PVs of -5 (black), -8 (cyan) and -10 (blue) (× $10^{-5}$ K.m$^2$.kg$^{-1}$.s$^{-1}$ at 530 K). The vertical red dashed lines correspond to the second derivative minima each year in the area delimited by a -10×$10^{-5}$ K.m$^2$.kg$^{-1}$.s$^{-1}$ PV contour.

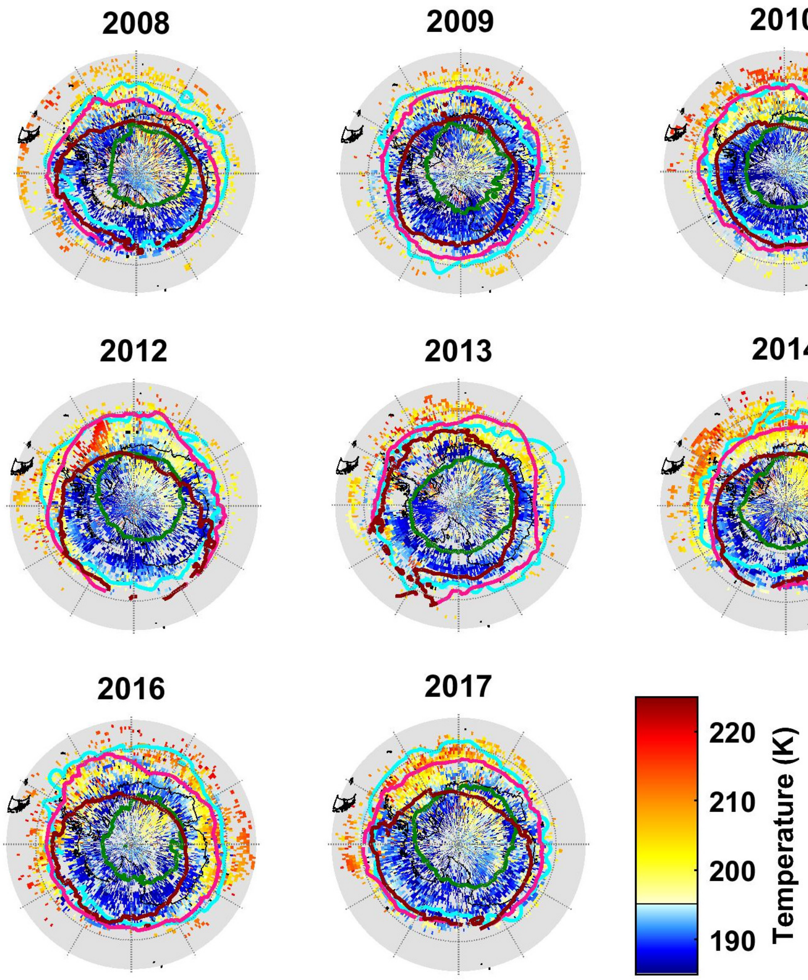


**Figure 7.** Spatial distribution (1°×1°) of the drop temperature at 50 hPa (K) (calculated from the total $HNO_3$ second derivative minima) for each year of IASI (2008–2017), in a region defined by a PV of $-8\times10^{-5}$ $K.m^2.kg^{-1}.s^{-1}$. The isocontours of $-10\times10^{-5}$ $K.m^2.kg^{-1}.s^{-1}$ at 530 K for the averaged PV (in green) and the minimum PV (in cyan) encountered over the period 10 May –15 July for each year and the isocontours of 195 K at 50 hPa for the averaged (in red) and the minimum (in pink) temperatures over the same period are represented.

## References


Braun, M., Grooß, J.-U., Woiwode, W., Johansson, S., Höpfner, M., Friedl-Vallon, F., Oelhaf, H., Preusse, P., Ungermann, J., Sinnhuber, B.-M., Ziereis, H., and Braesicke, P.: Nitrification of the lowermost stratosphere during the exceptionally cold Arctic winter 2015/16, Atmospheric Chemistry and Physics Discussions, https://doi.org/10.5194/acp-2019-108, 2019.

Carslaw, K. S., Luo, B. P., and Peter, T.: An analytical expression for the composition of aqueous {$HNO_3$-$H_2SO_4$-$H_2O$} stratospheric aerosols including gas phase removal of $HNO_3$, Geophys. Res. Lett., 22, 1877–1880, https://doi.org/10.1029/95GL01668, 1995.

Carslaw, K. S., Wirth, M., Tsias, A., Luo, B. P., Dörnbrack, A., Leutbecher, M., Volkert, H., Renger, W., Bacmeister, J. T., Reimer, E., and Peter, T.: Increased stratospheric ozone depletion due to mountain-induced atmospheric waves, Nature, 391, 675–678, https://doi.org/10.1038/35589, 1998.

Clerbaux, C., Boynard, A., Clarisse, L., George, M., Hadji-Lazaro, J., Herbin, H., Hurtmans, D., Pommier, M., Razavi, A., Turquety, S., Wespes, C., and Coheur, P.-F.: Monitoring of atmospheric composition using the thermal infrared IASI/MetOp sounder, Atmospheric Chemistry and Physics, 9, 6041–6054, https://doi.org/10.5194/acp-9-6041-2009, 2009.

de Laat, A. T. J. and van Weele, M.: The 2010 Antarctic ozone hole: Observed reduction in ozone destruction by minor sudden stratospheric warmings, Scientific Reports, 1, 38, https://doi.org/10.1038/srep00038, 2011.

de Zafra, R. and Smyshlyaev, S. P.: On the formation of HNO3 in the Antarctic mid to upper stratosphere in winter, Journal of Geophysical Research, 106, 23 115, https://doi.org/10.1029/2000JD000314, 2001.

Grooß, J. U., Engel, I., Borrmann, S., Frey, W., Günther, G., Hoyle, C. R., Kivi, R., Luo, B. P., Molleker, S., Peter, T., Pitts, M. C., Schlager, H., Stiller, G., Vömel, H., Walker, K. a., and Müller, R.: Nitric acid trihydrate nucleation and denitrification in the Arctic stratosphere, Atmospheric Chemistry and Physics, 14, 1055–1073, https://doi.org/10.5194/acp-14-1055-2014, 2014.

Hanson, D. and Mauersberger, K.: Laboratory studies of the nitric acid trihydrate: Implications for the south polar stratosphere, Geophysical Research Letters, 15, 855–858, https://doi.org/10.1029/GL015i008p00855, 1988.

Harris, N. R. P., Lehmann, R., Rex, M., and von der Gathen, P.: A closer look at Arctic ozone loss and polar stratospheric clouds, Atmospheric Chemistry and Physics, 10, 8499–8510, https://doi.org/10.5194/acp-10-8499-2010, 2010.

Hilton, F., Armante, R., August, T., Barnet, C., Bouchard, A., Camy-Peyret, C., Capelle, V., Clarisse, L., Clerbaux, C., Coheur, P.-F., Collard, A., Crevoisier, C., Dufour, G., Edwards, D., Faijan, F., Fourrié, N., Gambacorta, A., Goldberg, M., Guidard, V., Hurtmans, D., Illingworth, S., Jacquinet-Husson, N., Kerzenmacher, T., Klaes, D., Lavanant, L., Masiello, G., Matricardi, M., McNally, A., Newman, S., Pavelin, E., Payan, S., Péquignot, E., Peyridieu, S., Phulpin, T., Remedios, J., Schlüssel, P., Serio, C., Strow, L., Stubenrauch, C., Taylor, J., Tobin, D., Wolf, W., and Zhou, D.: Hyperspectral Earth Observation from IASI: Five Years of Accomplishments, Bulletin of the American Meteorological Society, 93, 347–370, https://doi.org/10.1175/BAMS-D-11-00027.1, 2012.

Hoffmann, L., Spang, R., Orr, A., Alexander, M. J., Holt, L. A., and Stein, O.: A decadal satellite record of gravity wave activity in the lower stratosphere to study polar stratospheric cloud formation, Atmospheric Chemistry and Physics, 17, 2901–2920, https://doi.org/10.5194/acp-17-2901-2017, 2017.

Höpfner, M., Luo, B. P., Massoli, P., Cairo, F., Spang, R., Snels, M., Di Donfrancesco, G., Stiller, G., von Clarmann, T., Fischer, H., and Biermann, U.: Spectroscopic evidence for NAT, STS, and ice in MIPAS infrared limb emission measurements of polar stratospheric clouds, Atmospheric Chemistry and Physics, 6, 1201–1219, https://doi.org/10.5194/acp-6-1201-2006, 2006.

Höpfner, M., Pitts, M. C., and Poole, L. R.: Comparison between CALIPSO and MIPAS observations of polar stratospheric clouds, Journal of Geophysical Research Atmospheres, 114, 1–15, https://doi.org/10.1029/2009JDO12114, 2009.

Hoyle, C. R., Engel, I., Luo, B. P., Pitts, M. C., Poole, L. R., Grooß, J. U., and Peter, T.: Heterogeneous formation of polar stratospheric clouds- Part 1: Nucleation of nitric acid trihydrate (NAT), Atmospheric Chemistry and Physics, 13, 9577–9595, https://doi.org/10.5194/acp-13- 9577-2013, 2013.

Hurtmans, D., Coheur, P.-F., Wespes, C., Clarisse, L., Scharf, O., Clerbaux, C., Hadji-Lazaro, J., George, M., and Turquety, S.: FORLI radiative transfer and retrieval code for IASI, Journal of Quantitative Spectroscopy and Radiative Transfer, 113, 1391–1408, https://doi.org/10.1016/j.jqsrt.2012.02.036, 2012.

James, A. D., Brooke, J. S. A., Mangan, T. P., Whale, T. F., Plane, J. M. C., and Murray, B. J.: Nucleation of nitric acid hydrates in polar stratospheric clouds by meteoric material, Atmospheric Chemistry and Physics, 18, 4519–4531, https://doi.org/10.5194/acp-18-4519- 2018, 2018.

Keys, J. G., Johnston, P. V., Blatherwick, R. D., and Murcray, F. J.: Evidence for heterogeneous reactions in the Antarctic autumn stratosphere, Nature, 361, 49–51, https://doi.org/10.1038/361049a0, 1993.

Klekociuk, A., Tully, M., Alexander, S., Dargaville, R., Deschamps, L., Fraser, P., Gies, H., Henderson, S., Javorniczky, J., Krummel, P., Petelina, S., Shanklin, J., Siddaway, J., and Stone, K.: The Antarctic ozone hole during 2010, Australian Meteorological and Oceanographic Journal, 61, 253–267, https://doi.org/10.22499/2.6104.006, 2011.

Koop, T., Luo, B., Tsias, A., and Peter, T.: Water activity as the determinant for homogeneous ice nucleation in aqueous solutions, Nature, 406, 611–614, https://doi.org/10.1038/35020537, 2000.

Lambert, A., Santee, M. L., Wu, D. L., and Chae, J. H.: A-train CALIOP and MLS observations of early winter Antarctic polar stratospheric clouds and nitric acid in 2008, Atmospheric Chemistry and Physics, 12, 2899–2931, https://doi.org/10.5194/acp-12-2899-2012, 2012.

Lambert, A., Santee, M. L., and Livesey, N. J.: Interannual variations of early winter Antarctic polar stratospheric cloud formation and nitric acid observed by CALIOP and MLS, Atmospheric Chemistry and Physics, 16, 15 219–15 246, https://doi.org/10.5194/acp-16-15219-2016, 2016.

Lambert, A. and Santee, M. L.: Accuracy and precision of polar lower stratospheric temperatures from reanalyses evaluated from A-Train CALIOP andMLS, COSMIC GPS RO, and the equilibrium thermodynamics of supercooled ternary solutions and ice clouds, Atmospheric Chemistry and Physics, 18, 1945–1975, https://doi.org/10.5194/acp-18-1945-2018, 2018.

Lowe, D. and MacKenzie, A. R.: Polar stratospheric cloud microphysics and chemistry, Journal of Atmospheric and Solar-Terrestrial Physics, 70, 13–40, https://doi.org/10.1016/j.jastp.2007.09.011, 2008.

Molleker, S., Borrmann, S., Schlager, H., Luo, B., Frey, W., Klingebiel, M., Weigel, R., Ebert, M., Mitev, V., Matthey, R., Woiwode, W., Oelhaf, H., Dörnbrack, A., Stratmann, G., Grooß, J.-U., Günther, G., Vogel, B., Müller, R., Krämer, M., Meyer, J., and Cairo, F.: Microphysical properties of synoptic-scale polar stratospheric clouds: in situ measurements of unexpectedly large HNO3-containing particles in the Arctic vortex, Atmospheric Chemistry and Physics, 14, 10 785–10 801, https://doi.org/10.5194/acp-14-10785-2014, 2014.

Murphy, D. M. and Koop, T.: Review of the vapour pressures of ice and supercooled water for atmospheric applications, Quarterly Journal of the Royal Meteorological Society, 131, 1539–1565, https://doi.org/10.1256/qj.04.94, 2005.

Peter, T.: Microphysics and heterogeneous chemistry of polar stratospheric clouds, Annual Review of Physical Chemistry, 48, 785–822, https://doi.org/10.1146/annurev.physchem.48.1.785, 1997.

Peter, T. and Grooß, J.-U.: Chapter 4. Polar Stratospheric Clouds and Sulfate Aerosol Particles: Microphysics, Denitrification and Heterogeneous Chemistry, in: Stratospheric Ozone Depletion and Climate Change, pp. 108–144, Royal Society of Chemistry, https://doi.org/10.1039/9781849733182-00108, 2012.

Piccolo, C. and Dudhia, A.: Precision validation of MIPAS-Envisat products, Atmospheric Chemistry and Physics, 7, 1915–1923, https://doi.org/10.5194/acp-7-1915-2007, 2007.

Pitts, M. C., Poole, L. R., Dörnbrack, A., and Thomason, L. W.: The 2009-2010 Arctic polar stratospheric cloud season: A CALIPSO perspective, Atmospheric Chemistry and Physics, 11, 2161–2177, https://doi.org/10.5194/acp-11-2161-2011, 2011.

Pitts, M. C., Poole, L. R., Lambert, A., and Thomason, L.W.: An assessment of CALIOP polar stratospheric cloud composition classification, Atmospheric Chemistry and Physics, 13, 2975–2988, https://doi.org/10.5194/acp-13-2975-2013, 2013.

Pitts, M. C., Poole, L. R., and Gonzalez, R.: Polar stratospheric cloud climatology based on CALIPSO spaceborne lidar measurements from 2006 to 2017, Atmospheric Chemistry and Physics, 18, 10 881–10 913, https://doi.org/10.5194/acp-18-10881-2018, 2018.

Rodgers, C. D.: Inverse Methods for Atmospheric Sounding - Theory and Practice, vol. 2 of Series on Atmospheric Oceanic and Planetary Physics, World Scientific Publishing Co. Pte. Ltd., https://doi.org/10.1142/9789812813718, 2000.

Roscoe, H. K., Feng, W., Chipperfield, M. P., Trainic, M., and Shuckburgh, E. F.: The existence of the edge region of the Antarctic stratospheric vortex, J. Geophys. Res., 117, D04301, doi:10.1029/2011JD015940, 2012.

Ronsmans, G., Langerock, B., Wespes, C., Hannigan, J. W., Hase, F., Kerzenmacher, T., Mahieu, E., Schneider, M., Smale, D., Hurtmans, D., De Mazière, M., Clerbaux, C., and Coheur, P.-F.: First characterization and validation of FORLI-HNO3 vertical profiles retrieved from IASI/Metop, Atmospheric Measurement Techniques, 9, 4783–4801, https://doi.org/10.5194/amt-9-4783-2016, 2016.

Ronsmans, G.,Wespes, C., Hurtmans, D., Clerbaux, C., and Coheur, P.-F.: Spatio-temporal variations of nitric acid total columns from 9 years of IASI measurements – a driver study, Atmospheric Chemistry and Physics, 18, 4403–4423, https://doi.org/10.5194/acp-18-4403-2018, 2018.

Santee, M. L., Manney, G. L., Froidevaux, L., Read, W. G., and Waters, J. W.: Six years of UARS Microwave Limb Sounder $HNO_3$ observations : Seasonal, interhemispheric, and interannual variations in the lower stratosphere, Journal of Geophysical Research, 104, 8225–8246, https://doi.org/10.1029/1998JD100089, 1999.

Santee, M. L., Lambert, A., Read, W. G., Livesey, N. J., Cofield, R. E., Cuddy, D. T., Daffer, W. H., Drouin, B. J., Froidevaux, L., Fuller, R. A., Jarnot, R. F., Knosp, B. W., Manney, G. L., Perun, V. S., Snyder, W. V., Stek, P. C., Thurstans, R. P., Wagner, P. A., Waters, J. W., Muscari, G., de Zafra, R. L., Dibb, J. E., Fahey, D. W., Popp, P. J., Marcy, T. P., Jucks, K. W., Toon, G. C., Stachnik, R. A., Bernath, P. F., Boone, C. D., Walker, K. A., Urban, J., and Murtagh, D.: Validation of the Aura Microwave Limb Sounder HNO3 measurements, Journal of Geophysical Research, 112, 1–22, https://doi.org/10.1029/2007JD008721, 2007.

Schreiner, J., Voigt, C., Weisser, C., Kohlmann, A., Mauersberger, K., Deshler, T., Kröger, C., Rosen, J., Kjome, N., Larsen, N., Adriani, A., Cairo, F., Donfrancesco, G. D., Ovarlez, J., Ovarlez, H., and Dörnbrack, A.: Chemical , microphysical , and optical properties of polar stratospheric clouds, Journal of Geophysical Research, 108, 1–10, https://doi.org/10.1029/2001JD000825, 2003.

Sheese, P. E., Walker, K. A., Boone, C. D., Bernath, P. F., Froidevaux, L., Funke, B., Raspollini, P., and von Clarmann, T.: ACE-FTS ozone, water vapour, nitrous oxide, nitric acid, and carbon monoxide profile comparisons with MIPAS and MLS, Journal of Quantitative Spectroscopy and Radiative Transfer, 186, 63–80, https://doi.org/10.1016/j.jqsrt.2016.06.026, 2017.

Snels, M., Scoccione, A., Liberto, L. D., Colao, F., Pitts, M., Poole, L., Deshler, T., Cairo, F., Cagnazzo, C., and Fierli, F.: Comparison of Antarctic polar stratospheric cloud observations by ground-based and space-borne lidar and relevance for chemistry–climate models, Atmospheric Chemistry and Physics, 19, 955–972, https://doi.org/10.5194/acp-19-955-2019, 2019.

Solomon, S.: Stratospheric ozone depletion: A review of concepts and history, Reviews of Geophysics, 37, 275–316, https://doi.org/10.1029/1999RG900008, 1999.

Spang, R., Hoffmann, L., Höpfner, M., Griessbach, S., Müller, R., Pitts, M. C., Orr, A. M. W., and Riese, M.: A multi-wavelength classification method for polar stratospheric cloud types using infrared limb spectra, Atmospheric Measurement Techniques, 9, 3619–3639, https://doi.org/10.5194/amt-9-3619-2016, 2016.

Spang, R., Hoffmann, L., Müller, R., Grooß, J.-U., Tritscher, I., Höpfner, M., Pitts, M., Orr, A., and Riese, M.: A climatology of polar stratospheric cloud composition between 2002 and 2012 based on MIPAS/Envisat observations, Atmospheric Chemistry and Physics, 18, 5089–5113, https://doi.org/10.5194/acp-18-5089-2018, 2018.

Toon, O. B., Hamill, P., Turco, R. P., and Pinto, J.: Condensation of HNO3 and HCl in the winter polar stratospheres, Geophysical Research Letters, 13, 1284–1287, https://doi.org/10.1029/GL013i012p01284, 1986.

Tritscher, I., Pitts, M. C., Poole, L. R., Alexander, S. P., Cairo, F., Chipperfield, M. P., et al.: Polar stratospheric clouds: Satellite observations, processes, and role in ozone depletion, Reviews of Geophysics, 59, e2020RG000702, https://doi.org/10.1029/2020RG000702.

Urban, J., Pommier, M., Murtagh, D. P., Santee, M. L., and Orsolini, Y. J.: Nitric acid in the stratosphere based on Odin observations from 2001 to 2009 – Part 1: A global climatology, Atmospheric Chemistry and Physics, 9, 7031–7044, https://doi.org/10.5194/acp-9-7031- 2009, 2009.

Voigt, C., Schreiner, J., Kohlmann, A., Zink, P., Mauersberger, K., Larsen, N., Deshler, T., Kro, C., Rosen, J., Adriani, A., Cairo, F., Donfrancesco, G. D., Viterbini, M., Ovarlez, J., Ovarlez, H., and David, C.: Nitric Acid Trihydrate (NAT) in Polar Stratospheric Clouds, Science, 290, 1756–1758, https://doi.org/10.1126/science.290.5497.1756, 2000.

Voigt, C., Larsen, N., Deshler, T., et al.: In situ mountainwave polar stratospheric cloud measurements: Implications for nitric acid trihydrate formation, J. Geophys. Res., 108(D5), doi:10.1029/2001JD001185, 2003.

Voigt, C., Schlager, H., Luo, B. P., Dörnbrack, A., Roiger, A., Stock, P., Curtius, J., Vössing, H., Borrmann, S., Davies, S., Konopka, P., Schiller, C., Shur, G., and Peter, T.: Nitric Acid Trihydrate (NAT) formation at low NAT supersaturation in Polar Stratospheric Clouds (PSCs), Atmospheric Chemistry and Physics, 5, 1371–1380, https://doi.org/10.5194/acp-5-1371-2005, 2005.

von König, M.: Using gas-phase nitric acid as an indicator of PSC composition, Journal of Geophysical Research, 107, https://doi.org/10.1029/2001jd001041, 2002.

Wang, X. and Michelangeli, D. V.: A review of polar stratospheric cloud formation, China Particuology, 4, 261–271, https://doi.org/10.1016/S1672-2515(07)60275-9, 2006.

Wegner, T., Grooß, J.-U., von Hobe, M., Stroh, F., Sumin´ska-Ebersoldt, O., Volk, C. M., Hösen, E., Mitev, V., Shur, G., and Müller, R.: Heterogeneous chlorine activation on stratospheric aerosols and clouds in the Arctic polar vortex, Atmospheric Chemistry and Physics, 12, 11 095–11 106, https://doi.org/10.5194/acp-12-11095-2012, 2012.

Wespes, C., Hurtmans, D., Clerbaux, C., and Coheur, P.-F.: $O_3$ variability in the troposphere as observed by IASI over 2008-2016: Contribution of atmospheric chemistry and dynamics, Journal of Geophysical Research: Atmospheres, 122, 2429–2451, https://doi.org/10.1002/2016JD025875, http://doi.wiley.com/10.1002/2016JD025875, 2017.

WMO: Scientific Assessment of Ozone Depletion: 2014, Global Ozone Research and Monitoring Project – Report No. 55, World Meteorological Organization, Geneva, Switzerland, 2014.

Zhu, Y., Toon, O. B., Lambert, A., Kinnison, D. E., Brakebusch, M., Bardeen, C. G., Mills, M. J., and English, J. M.: Development of a Polar Stratospheric Cloud Model within the Community Earth System Model using constraints on Type I PSCs from the 2010-2011 Arctic winter, Journal of Advances in Modeling Earth Systems, 7, 551–585, https://doi.org/10.1002/2015ms000427, 2015.

Zondlo, M. A., P. K. Hudson, A. J. Prenni, and M. A. Tolbert: Chemistry and microphysics of polar stratospheric clouds and cirrus clouds, Annu. Rev. Phys. Chem., 51, 473–499, 2000.